

Supplementary material: Extreme Non-Reciprocal Near-Field Thermal Radiation via Floquet Photonics

Lucas J. Fernández-Alcázar¹, Rodion Kononchuk¹, Huanan Li², Tsampikos Kottos¹

¹*Wave Transport in Complex Systems Lab, Department of Physics,
Wesleyan University, Middletown, CT-06459, USA*

²*Photonics Initiative, Advanced Science Research Center, CUNY, NY 10031, USA*

(Dated: April 15, 2021)

ENERGY CURRENT AND FLOQUET SCATTERING MATRIX

In this section, we provide a derivation for the net average energy current \bar{I}_α directed toward a heat bath α , i.e., Eq. (4) of the main text, when a scatterer connecting thermal reservoirs is periodically driven. We start by considering the waves $|\psi(t)\rangle$ inside the scatterer, evolving according to the equation

$$\frac{d|\psi(t)\rangle}{dt} = [iH(t) - \Gamma] |\psi(t)\rangle + D^+ |S_+(t)\rangle. \quad (\text{S1})$$

The field amplitude $|\psi(t)\rangle$ results from the excitations $|S_+(t)\rangle$ coming from the heat baths connected to the system through the (frequency-independent) coupling matrix D . The time dependent Hamiltonian $H(t)$ and the losses $\Gamma = DD^+/2$ not only determine the dynamics of the wave function, but also shape the outgoing scattered waves

$$|S_-(t)\rangle = -|S_+(t)\rangle + D |\psi(t)\rangle. \quad (\text{S2})$$

These complex quantities, in coupled mode theory, are represented in the frequency domain through their positive frequency component $|f(t)\rangle = \int_0^\infty d\omega |f(\omega)\rangle e^{i\omega t}$ and $|f(\omega)\rangle = |f(-\omega)\rangle^* = \int_{-\infty}^{+\infty} |f(t)\rangle e^{-i\omega t} dt / (2\pi)$; $\omega > 0$ where f is S_\pm or ψ . The effective Hamiltonian, being periodic in time, results

$$H_{\text{eff}}(t) = H_{\text{eff}}(t + \frac{2\pi}{\Omega}) = H(t) + i\Gamma = \sum_{m=-\infty}^{+\infty} e^{im\Omega t} H_Q^{0,(m)}, \quad (\text{S3})$$

where Ω is the modulation frequency and $H_Q^{0,(m)} = \frac{\Omega}{2\pi} \int_0^{2\pi/\Omega} H_{\text{eff}}(t) e^{-im\Omega t} dt$ is a $N_S \times N_S$ matrix, with N_S being the number of modes. In what follows, we assume that Eq. (S1) is valid around a resonant frequency ω_0 , and $|\psi(\omega)\rangle \rightarrow 0$ when $\omega \gg \omega_0$ or $\omega \ll \omega_0$ and that $\Omega \ll \omega_0$. In addition, the thermal excitations coming from bath β , $S_\beta^+(\omega) = \langle \beta | S_+(\omega) \rangle$, satisfy the correlation relation

$$\langle [S_{\beta'}^+(\omega')]^* S_\beta^+(\omega) \rangle = \frac{\tilde{\Theta}_\beta(\omega)}{2\pi} \delta_{\beta',\beta} \delta(\omega - \omega'), \quad (\text{S4})$$

where $\tilde{\Theta}_\beta(\omega) = \hbar\omega\phi_\beta(\omega)[\exp(\hbar\omega/(k_B T_\beta)) - 1]^{-1}$, $\phi_\alpha(\omega)$ is the spectral filtering function, k_B is the Boltzmann constant and T_β is temperature of reservoir β . Therefore, from Eq. (S1) we have

$$\omega |\psi(\omega)\rangle = \sum_m H_Q^{0,(m)} |\psi(\omega - m\Omega)\rangle - iD^T |S_+(\omega)\rangle. \quad (\text{S5})$$

We can turn Eq. (S5) into a matrix equation in an extended space

$$([\hat{\omega}] - \hat{H}_Q) \vec{\psi}(\hat{\omega}) = -i[D]^T \vec{S}_+(\hat{\omega}), \quad (\text{S6})$$

with the definition of the following quantities. The block matrix $\hat{H}_Q = H_Q^0 - [n\Omega]$, where H_Q^0 and $[n\Omega]$ are block matrices, whose blocks are $(H_Q^0)_{p,q} = H_Q^{0,(q-p)}$ and $[n\Omega] = \text{diag}\{\dots, \Omega I_{N_S}, 0, -\Omega I_{N_S}, \dots\}$, respectively. Here, I_{N_S} is the $N_S \times N_S$ identity matrix and the notation $[A]$ represents a block diagonal matrix whose blocks are $A I_{N_S}$. We denote the frequency as $\hat{\omega}$ when its range is restricted to $\hat{\omega} \in [\omega_0 - \Omega/2, \omega_0 + \Omega/2]$. Finally, we define the vectors $\vec{f} = [\dots, |f(\hat{\omega}_{+1})\rangle, |f(\hat{\omega}_0)\rangle, |f(\hat{\omega}_{-1})\rangle, \dots]^T$, with f being, as before, S_\pm or ψ , and where $\hat{\omega}_n = \hat{\omega} + n\Omega$.

Interestingly, Eq. (S6) allow us to express the wave function vector in a physically meaningful form,

$$\vec{\psi}(\hat{\omega}) = -iG^F[D]^T \vec{S}_+(\hat{\omega}), \quad (\text{S7})$$

which evidences that the excitations introduced by the thermal baths, $\vec{S}_+(\hat{\omega})$, are propagated through the system in the extended dimension, and hence scattered to other frequencies. The propagator,

$$G^F = \left([\hat{\omega}] - \hat{H}_Q \right)^{-1}, \quad (\text{S8})$$

is nothing else than the Green's function of the extended space, or also called Floquet Green's function, which allow us to find the outgoing scattered fields for given incident waves $\vec{S}_+(\hat{\omega})$.

The above mentioned outgoing scattered field can be readily found by using the Fourier transform of Eq. (S2) in the extended space and Eq. (S7),

$$\begin{aligned} \vec{S}_-(\hat{\omega}) &= -\vec{S}_+(\hat{\omega}) + [D]\vec{\psi}(\hat{\omega}), \\ &= (-I - i[D]G^F[D]^T)\vec{S}_+(\hat{\omega}), \end{aligned} \quad (\text{S9})$$

where $\mathbf{I} = [1]$. Here, we identify the term inside the parenthesis as the Floquet Scattering matrix

$$\mathcal{S}^F = -I - i[D]G^F[D]^T, \quad (\text{S10})$$

and this allow us to find the scattered field going out of the system toward lead α

$$S_{\alpha n}^-(\hat{\omega}) = \sum_{\beta, m} \mathcal{S}_{\alpha n, \beta m}^F(\hat{\omega}) S_{\beta m}^+(\hat{\omega}), \quad (\text{S11})$$

where $S_{\beta}^{\pm}(\hat{\omega}_m) = S_{\beta m}^{\pm}(\hat{\omega}) = \langle \beta | S_{\pm}(\hat{\omega} + m\Omega) \rangle$. Notice that the element $\mathcal{S}_{\alpha n, \beta m}^F(\hat{\omega})$ indicates that radiation coming from lead β at frequency $\hat{\omega}_m = \hat{\omega} + m\Omega$ leaves the system toward lead α with frequency $\hat{\omega}_n = \hat{\omega} + n\Omega$. Then, in order to highlight the incident and outgoing frequencies, we will also use the notation $\mathcal{S}_{\alpha, \beta}^F(\hat{\omega}_n, \hat{\omega}_m) \equiv \mathcal{S}_{\alpha n, \beta m}^F(\hat{\omega})$.

The net average energy current going out of the system toward the reservoir α is

$$\bar{I}_{\alpha}^{out} = \frac{\Omega}{2\pi} \int_0^{2\pi/\Omega} dt \langle |S_{\alpha}^-(t)|^2 \rangle, \quad (\text{S12})$$

where the outgoing field in the frequency domain can be written as

$$S_{\alpha}^-(t) = \sum_n \int_{\omega_0 - \frac{\Omega}{2}}^{\omega_0 + \frac{\Omega}{2}} S_{\alpha n}^-(\hat{\omega}) e^{i(\hat{\omega} + n\Omega)t} d\hat{\omega}. \quad (\text{S13})$$

Introducing Eq. (S13) into Eq. (S12) leads us to evaluate the correlation for the outgoing scattered fields, which read

$$\begin{aligned} \langle (S_{\alpha n}^-(\hat{\omega}))^* S_{\alpha n'}^-(\hat{\omega}') \rangle &= \sum_{\beta, m} (\mathcal{S}_{\alpha n, \beta m}^F(\hat{\omega}))^* \mathcal{S}_{\alpha n', \beta m}^F(\hat{\omega}') \times \\ &\times \frac{\tilde{\Theta}_{\beta}(\hat{\omega} + m\Omega)}{2\pi} \delta(\hat{\omega} - \hat{\omega}'). \end{aligned} \quad (\text{S14})$$

Here we have used Eqs. (S11), (S13), and the correlation relations for the incident radiation

$$\langle (S_{\beta m}^+(\hat{\omega}))^* S_{\beta' m'}^+(\hat{\omega}') \rangle = \frac{\tilde{\Theta}_{\beta}(\hat{\omega} + m\Omega)}{2\pi} \delta_{\beta, \beta'} \delta_{m, m'} \delta(\hat{\omega} - \hat{\omega}'), \quad (\text{S15})$$

which follow from the properties of the thermal reservoirs, Eq. (S4). Therefore, we obtain

$$\begin{aligned} \bar{I}_{\alpha}^{out} &= \sum_n \int_{\omega_0 - \frac{\Omega}{2}}^{\omega_0 + \frac{\Omega}{2}} \frac{d\hat{\omega}}{2\pi} \sum_{\beta, m} |\mathcal{S}_{\alpha n, \beta m}^F(\hat{\omega})|^2 \tilde{\Theta}_{\beta}(\hat{\omega} + m\Omega) \\ &= \int_0^{\infty} \frac{d\omega}{2\pi} \sum_{\beta, m} |\mathcal{S}_{\alpha, \beta}^F(\omega, \omega + m\Omega)|^2 \tilde{\Theta}_{\beta}(\omega + m\Omega) \end{aligned} \quad (\text{S16})$$

where we have used $\frac{\Omega}{2\pi} \int_0^{2\pi/\Omega} dt e^{i(n' - n)\Omega t} = \delta_{n', n}$. Notice that in Eq. (S16) we have restored the integration over the whole frequency range by using the incident-outgoing frequency notation for \mathcal{S}^F .

Finally, we can evaluate the net average energy current going toward reservoir α

$$\bar{I}_\alpha = -\bar{I}_\alpha^{in} + \bar{I}_\alpha^{out}, \quad (\text{S17})$$

where the incident energy current $\bar{I}_\alpha^{in} = \frac{\Omega}{2\pi} \int_0^{2\pi/\Omega} dt \langle |S_\alpha^+(t)|^2 \rangle = \int_0^\infty \frac{d\omega}{2\pi} \tilde{\Theta}_\alpha(\omega)$. Finally, using Eq. (S16) and shifting $\omega_m \rightarrow \omega$, we obtain

$$\bar{I}_\alpha = \int_0^\infty \frac{d\omega}{2\pi} \sum_{\beta n} \left[-\delta_{\beta,\alpha} \delta_{n,0} + |S_{\alpha\beta}^F(\omega + n\Omega, \omega)|^2 \right] \tilde{\Theta}_\beta(\omega), \quad (\text{S18})$$

which demonstrates Eq. (4) of the main text. Notice that, \bar{I}_α is defined as positive when the current is going toward the reservoir α .

ENERGY CURRENT IN THE ADIABATIC LIMIT.

Here, we provide an expression for the average energy current valid for adiabatic modulations, $\Omega \rightarrow 0$, and small temperature gradients without involving the classical limit. Further details will be given in a future publication[S1]. The average energy current at a lead 2 can be separate in two contributions, as in Eq. (6) of the main text,

$$\bar{I}_2 \approx \bar{I}_{2,b} + \bar{I}_{2,p}. \quad (\text{S19})$$

Here, the bias current reads

$$\bar{I}_{2,b} = \int \frac{d\omega}{2\pi} \hbar \omega \bar{\mathcal{T}}(\omega) (\Theta_1(\omega) - \Theta_2(\omega)), \quad (\text{S20})$$

where the transmittance $\bar{\mathcal{T}}(\omega) = \frac{\Omega}{2\pi} \int dt |S_{21}^t(\omega)|^2$ is averaged over one cycle, being S^t the instantaneous scattering matrix, and we consider instantaneous reciprocal transport, i.e. $S_{21}^t(\omega) = S_{12}^t(\omega)$, and filtering function $\phi_\beta(\omega) \equiv 1$. The current associated with the modulation of the scatterer is the pumped current that, evaluated at lead 2, reads

$$\bar{I}_{2,p}^{(f)} \approx \frac{\Omega}{2\pi} \int \frac{d\omega}{2\pi} \hbar \left[\omega \Theta_0(\omega) \frac{\partial P_{22}}{\partial \omega} + P_{22}(\omega) \Theta_0(\omega) \right], \quad (\text{S21})$$

where $\Theta_0(\omega) = [\exp(\hbar\omega/(k_B T_0)) - 1]^{-1}$ is associated to a mean temperature $T_0 = (T_1 + T_2)/2$, and $P_{22}(\omega) = \int dt \left(\frac{dS^t}{dt}(S^t)^\dagger \right)_{2,2}$. In the classical limit, where $\Theta_0(\omega) \approx k_B T_0/(\hbar\omega)$, integration of the first term of Eq. (S21) results proportional to $[P_{22}(\omega)]_0^\infty \approx 0$ and, thus, we arrive to the second line of Eq. (7) of the main text. We point out that, to arrive to Eq. (S21), we neglected terms of order $\mathcal{O}(\Omega^2, (\Delta T/T_0)^2, \Omega \Delta T/T_0)$ and higher.

DECIMATION PROCEDURES, EFFECTIVE HAMILTONIANS, AND GREEN'S FUNCTIONS

The main difficulty in the computation of S^F in Eq. (3) of the main text is associated with the evaluation of the Floquet Green's function $G^F = ([\omega] - \hat{H}_Q)^{-1}$, which requires the inversion of the matrix $([\omega] - \hat{H}_Q)$ whose rank is in principle infinite involving all Floquet channels $n \in (-\infty, +\infty)$. Approximate results can be obtained through truncations of the Floquet space to $n \in [-N_F, N_F]$, where reliable results require N_F to be large, slowing down the calculation.

Of course, there are cases, e.g. slow and high modulation frequencies [S2–S4] or a simple two-mode Rabi driving schemes [S5], where G^F and subsequently \bar{I}_α are easily calculated. In most general scenarios, however, one needs to consider many Floquet channels in order to obtain an accurate description of the scattering process. We have tackled this difficulty by employing a decimation technique borrowed from the field of molecular electronics [S6–S8]. By utilizing the block diagonal structure of the Hamiltonian in the Floquet -Hilbert space, a matrix continued fraction expansion [S8] enables the calculation of G^F via an iteration relation connecting blocks n and m .

Floquet Hamiltonians \hat{H}_Q have typically a block structure. In particular, for simple driving schemes (few harmonics in the Fourier expansion of the effective Hamiltonian) \hat{H}_Q is block tridiagonal and thus several nondiagonal blocks are zeros. Here, we take advantage of this structure and we perform efficient calculation of G^F by means of the *decimation* procedures, inspired in the renormalization group techniques of statistical mechanics [S6], and widely

utilized in Condensed Matter [S8] and Molecular Electronics [S7]. Here we will show the basics of this technique, and we parallel the approach given in Refs. [S7, S8].

The decimation procedures recursively reduce a general $N \times N$ Hamiltonian into another of lower rank by decreasing the number of degrees of freedom, without altering its physical properties. As a result, the method utilizes $\mathcal{O}(N)$ operations instead of $\mathcal{O}(N^2)$ required by the matrix inversion [S8] and allow us to deal with complex driving schemes which are intractable by any other method. For instructive purposes, let us consider a block tridiagonal Hamiltonian \mathbb{H} such that it satisfies the equation

$$\begin{bmatrix} \omega - \mathbb{E}_1 & -\mathbb{V}_{12} & \mathbb{O} \\ -\mathbb{V}_{21} & \omega - \mathbb{E}_2 & -\mathbb{V}_{23} \\ \mathbb{O} & -\mathbb{V}_{32} & \omega - \mathbb{E}_3 \end{bmatrix} \begin{pmatrix} \vec{u}_1 \\ \vec{u}_2 \\ \vec{u}_3 \end{pmatrix} = [\omega - \mathbb{H}] \vec{u} = \vec{0}, \quad (\text{S22})$$

where the corresponding identity matrices multiplying ω are implicit. From the middle (block) equation, we can isolate \vec{u}_2 and *decimate* it, leading to the equations

$$\begin{bmatrix} \omega - \bar{\mathbb{E}}_1 & -\bar{\mathbb{V}}_{13} \\ -\bar{\mathbb{V}}_{31} & \omega - \bar{\mathbb{E}}_3 \end{bmatrix} \begin{pmatrix} \vec{u}_1 \\ \vec{u}_3 \end{pmatrix} = [\omega - \mathbb{H}_{\text{eff}}] \vec{u} = 0. \quad (\text{S23})$$

Here, the blocks have been renormalized hiding the (nonlinear) dependence on ω :

$$\begin{aligned} \bar{\mathbb{E}}_1 &= \mathbb{E}_1 + \Sigma_1(\omega) = \mathbb{E}_1 + \mathbb{V}_{12} (\omega - \mathbb{E}_2)^{-1} \mathbb{V}_{21}, \\ \bar{\mathbb{E}}_3 &= \mathbb{E}_3 + \Sigma_3(\omega) = \mathbb{E}_3 + \mathbb{V}_{32} (\omega - \mathbb{E}_2)^{-1} \mathbb{V}_{23}, \\ \bar{\mathbb{V}}_{13} &= \mathbb{V}_{12} \frac{1}{\omega - \mathbb{E}_2} \mathbb{V}_{23}; \quad \bar{\mathbb{V}}_{31} = \mathbb{V}_{32} \frac{1}{\omega - \mathbb{E}_2} \mathbb{V}_{21}. \end{aligned} \quad (\text{S24})$$

The terms $\Sigma_j(\omega)$, known as self-energies, account for the frequency (energy) shifts due to the coupling with the decimated state. Notice that now, there are effective coupling elements $\bar{\mathbb{V}}_{13(31)}$ between blocks 1 and 3 accounting for the interaction of those blocks mediated by the decimated block 2. Importantly, the nonlinear dependence on ω codifies all information on the steady state scattering as well as on the dynamics. For instance, Eq. (S23) gives the exact spectrum of the whole system.

Now, let us come back to Eq. (S22) and decimate block 3 and then 2. According to Eq. (S24), now we have only block 1, which is renormalized as

$$\begin{aligned} \tilde{\mathbb{E}}_1 &= \mathbb{E}_1 + \Sigma_1^{(3)}(\omega) \\ &= \mathbb{E}_1 + \mathbb{V}_{12} \left(\omega - \mathbb{E}_2 - \Sigma_2^{(3)} \right)^{-1} \mathbb{V}_{21} \\ &= \mathbb{E}_1 + \mathbb{V}_{12} \left[\omega - \mathbb{E}_2 - \mathbb{V}_{23} (\omega - \mathbb{E}_3)^{-1} \mathbb{V}_{32} \right]^{-1} \mathbb{V}_{21} \end{aligned} \quad (\text{S25})$$

Here, we have introduced the notation $\Sigma_n^{(m)}$ to indicate the correction to block n due to the decimation of all blocks between n and m , with m included. We highlight that the order of the decimation protocol does not affect $\Sigma_n^{(m)}$, which is obtained as “matrix continued fractions” [S8].

The recursive structure of the self-energy $\Sigma_n^{(m)}$, e.g. as shown in Eq. (S25), can be used to efficiently reduce Hamiltonians of arbitrary dimensions. In particular, the Floquet Hamiltonian can be decimated into two blocks, with labels n and m , resulting in

$$\begin{aligned} \tilde{\mathbb{E}}_n &= \mathbb{E}_n + \Sigma_n^{(1)} + \Sigma_n^{(m)} \\ \tilde{\mathbb{E}}_m &= \mathbb{E}_m + \Sigma_m^{(N)} + \Sigma_m^{(n)} \\ \tilde{\mathbb{V}}_{n,m} &= \tilde{\mathbb{V}}_{n,m-1} (\omega - \mathbb{E}_m - \Sigma_m^{(n)})^{-1} \mathbb{V}_{m-1,m} \end{aligned} \quad (\text{S26})$$

where

$$\begin{aligned} \Sigma_n^{(m)} &= \left[\mathbb{V}_{n,n+1} \left(\omega - \mathbb{E}_{n+1} - \Sigma_{n+1}^{(m)} \right)^{-1} \right] \mathbb{V}_{n+1,n} \\ \Sigma_m^{(n)} &= \left[\mathbb{V}_{m,m-1} \left(\omega - \mathbb{E}_{m-1} - \Sigma_{m-1}^{(n)} \right)^{-1} \right] \mathbb{V}_{m-1,m} \end{aligned} \quad (\text{S27})$$

for $m > n$. We have assumed block tridiagonal matrices, but the procedure can be straightforwardly generalized to address other situations.

Now, utilizing this procedure, we can address our initial question by obtaining the block element of the total Green's function connecting blocks n and m from

$$\begin{bmatrix} \mathbb{G}_{nn} & \mathbb{G}_{nm} \\ \mathbb{G}_{mn} & \mathbb{G}_{mm} \end{bmatrix} = \begin{bmatrix} \omega - \tilde{\mathbb{E}}_n & -\tilde{\mathbb{V}}_{nm} \\ -\tilde{\mathbb{V}}_{mn} & \omega - \tilde{\mathbb{E}}_m \end{bmatrix}^{-1}. \quad (\text{S28})$$

The inversion of the matrix can be performed resorting to the block-inversion matrix

$$\begin{aligned} \begin{bmatrix} \mathbb{A} & \mathbb{B} \\ \mathbb{C} & \mathbb{D} \end{bmatrix}^{-1} &= \\ &= \begin{bmatrix} (\mathbb{A} - \mathbb{B}\mathbb{D}^{-1}\mathbb{C})^{-1} & -(\mathbb{A} - \mathbb{B}\mathbb{D}^{-1}\mathbb{C})^{-1}\mathbb{B}\mathbb{D}^{-1} \\ -(\mathbb{D} - \mathbb{C}\mathbb{A}^{-1}\mathbb{B})^{-1}\mathbb{C}\mathbb{A}^{-1} & (\mathbb{D} - \mathbb{C}\mathbb{A}^{-1}\mathbb{B})^{-1} \end{bmatrix}, \end{aligned} \quad (\text{S29})$$

which requires the existence of the inverses of matrices \mathbb{D} , \mathbb{A} , $(\mathbb{D} - \mathbb{C}\mathbb{A}^{-1}\mathbb{B})$, and $(\mathbb{A} - \mathbb{B}\mathbb{D}^{-1}\mathbb{C})$. In our case, all of them exist. Therefore we have,

$$\begin{aligned} \mathbb{G}_{nn} &= \left[(\omega - \mathbb{E}_n) - \Sigma_n^{(1)} - \Sigma_n^{(N)} \right]^{-1}, \\ \mathbb{G}_{mm} &= \left[(\omega - \mathbb{E}_m) - \Sigma_m^{(1)} - \Sigma_m^{(N)} \right]^{-1}, \\ \mathbb{G}_{nm} &= \mathbb{G}_{nn} \left[\tilde{\mathbb{V}}_{nm} (\omega - \tilde{\mathbb{E}}_m)^{-1} \right], \\ \mathbb{G}_{mn} &= \mathbb{G}_{mm} \left[\tilde{\mathbb{V}}_{mn} (\omega - \tilde{\mathbb{E}}_n)^{-1} \right]. \end{aligned} \quad (\text{S30})$$

These equations allow the calculation of the Green's functions avoiding the inversion of the full Floquet Hamiltonian matrix. In Eq. (S30) the recursive nature of the decimation procedure requires $\mathcal{O}(N)$ self energies $\Sigma_n^{(1)}$ and $\Sigma_n^{(N)}$ for the diagonal elements of G^F . For the nondiagonal elements, it is possible to use the self energies already calculated for the diagonal ones, highly improving the performance of the method.[S8]

COUPLED MODE THEORY DESCRIPTION OF THE ELECTRICAL CIRCUITS

We construct a CMT description for the electrical circuit as shown in Fig. 1(c,d). As a first step, we analyze a LC resonator using a complex mode amplitude ψ . Specifically, we define the mode amplitude $\psi(t)$ to be $\psi(t) \equiv \sqrt{C/2} [v(t) + \dot{v}(t)/(j\omega_0)]$ in terms of the node voltage $v(t)$ and its time derivative $\dot{v}(t)$, where $\omega_0 = 1/\sqrt{LC}$ is the resonant (angular) frequency of the LC resonator. The definition of the mode amplitude ψ allows us to rewrite the circuit equation, i.e., $\frac{d^2 v(t)}{dt^2} + \omega_0^2 v(t) = 0$, equivalently as the first-order differential equation $\frac{d}{dt} \psi(t) = j\omega_0 \psi(t)$ or its complex conjugate. At the same time, the mode amplitude ψ is normalized such that $|\psi|^2$ represents the energy stored in the resonator. Notice that the full degree of freedom i.e., $v(t)$ and $\dot{v}(t)$, required to specify the circuits completely at each time, is maintained in the complex-mode description, since they can be expressed, using the definition of the amplitude $\psi(t)$ and its complex conjugate $\psi^*(t)$, as $v(t) = \frac{1}{\sqrt{2C}} [\psi(t) + \psi^*(t)]$ and $\dot{v}(t) = j\omega_0 \frac{1}{\sqrt{2C}} [\psi(t) - \psi^*(t)]$. Nevertheless, when describing the dynamics of circuits, the amplitude $\psi(t)$ and its complex conjugate $\psi^*(t)$ are generally not decoupled with each other as seen below.

We proceed to describe the coupling between two (identical) LC resonators under the complex-mode description. As considered in Fig. 1(c,d), the coupling between the resonators can be enabled by the capacitor $C_c = \kappa C$. According to Kirchhoff's laws, the circuit equations describing the coupled LC resonators simply read

$$(1 + \kappa) \frac{d^2 v_1}{dt^2} - \kappa \frac{d^2 v_2}{dt^2} + \omega_0^2 v_1 = 0, \quad (\text{S31})$$

$$(1 + \kappa) \frac{d^2 v_2}{dt^2} - \kappa \frac{d^2 v_1}{dt^2} + \omega_0^2 v_2 = 0 \quad (\text{S32})$$

where $v_n, n = 1, 2$ are the node voltages of each resonator. Using the complex-mode representation ψ_n for each resonator n , we can rewrite the circuit equations Eq. (S31) and (S32) as

$$\frac{d\psi_1}{dt} \approx j\omega_0 \psi_1 - \frac{j\omega_0}{2} \kappa (\psi_1 - \psi_2 + \psi_1^* - \psi_2^*) \quad (\text{S33})$$

$$\frac{d\psi_2}{dt} \approx j\omega_0 \psi_2 - \frac{j\omega_0}{2} \kappa (\psi_2 - \psi_1 + \psi_2^* - \psi_1^*) \quad (\text{S34})$$

when assuming $\kappa \rightarrow 0$. Furthermore, under the rotating-wave approximation enabled by the weak coupling $\kappa \rightarrow 0$, we can simplify the Eqs. (S33) and (S34) further by decoupling ψ_n with their complex conjugates ψ_n^* to get a coupled mode form

$$\frac{d\psi_1}{dt} \approx j\omega_0 \left(1 - \frac{1}{2}\kappa\right) \psi_1 + \frac{j\omega_0}{2}\kappa\psi_2 \quad (\text{S35})$$

$$\frac{d\psi_2}{dt} \approx \frac{j\omega_0}{2}\kappa\psi_1 + j\omega_0 \left(1 - \frac{1}{2}\kappa\right) \psi_2. \quad (\text{S36})$$

Clearly, the capacitive coupling $C_e = \kappa C$ shifts the resonant frequency of each resonators in addition to coupling the two resonators.

The effects of the external capacitive coupling $C_e = \epsilon C$ between a transmission line (TL) and a LC resonator can be examined similarly. Before that, we need to define the complex wave amplitude S^\pm for the incoming/outgoing wave flowing through the TL. Along the TL, the voltage $v(z, t)$ and current $i(z, t)$ can be written in terms of the superposition of incoming and outgoing voltage waves $v^+(z, t)$ and $v^-(z, t)$ as $v(z, t) = v^+(z, t) + v^-(z, t)$ and $i(z, t) = i^+(z, t) + i^-(z, t) = v^+(z, t)/Z_0 - v^-(z, t)/Z_0$, where Z_0 is the characteristic impedance of TL. In turn, the real voltage waves $v^\pm(z, t)$ can be separated into the complex wave amplitude $S^\pm(z, t)$ and its complex conjugate as $v^\pm(z, t) = \sqrt{\frac{Z_0}{2}} [S^\pm(z, t) + S^\pm(z, t)^*]$. We assume that $S^\pm(z, t) = \tilde{S}^\pm(z, t) e^{j\omega_0 t}$ with a slow envelope $\tilde{S}^\pm(z, t)$ such that $\frac{\partial S^\pm}{\partial t} \approx j\omega_0 S^\pm$. Correspondingly, the time-averaged incoming and outgoing power with respect to the period $2\pi/\omega_0$, i.e., $P^\pm = \langle v^\pm i^\pm \rangle$, are simply $\pm |S^\pm|^2$, benefiting from the proper normalization factor in the definition of wave amplitudes. From now on, we will use $S^\pm(t)$ to represent the incoming and outgoing wave amplitude at the ending position $z = 0$ of the TL, where the external coupling capacitor C_e is attached. The set of circuit equations accounting for the coupling between the TL and the LC resonator are

$$i(0, t) = C_e \frac{d}{dt} [v(0, t) - v] \quad (\text{S37})$$

$$\frac{di(0, t)}{dt} = C \frac{d^2 v}{dt^2} + \frac{v}{L} \quad (\text{S38})$$

where v is the node voltage of the LC resonator. Assuming that $Z_0 \sim O(z_0)$ with $z_0 \equiv \sqrt{L/C}$ and $\epsilon \rightarrow 0$ for the weak coupling, we can use the complex mode amplitude ψ of the resonator and the input/output wave amplitude S^\pm to reformulate Eqs. (S37) and (S38) as

$$S^- \approx S^+ + j\sqrt{\omega_0 r \epsilon} \psi \quad (\text{S39})$$

$$\frac{d\psi}{dt} \approx j\omega_0 \left(1 - \frac{1}{2}\epsilon\right) \psi - \frac{1}{2}\omega_0 r \epsilon^2 \psi + j\sqrt{\omega_0 r \epsilon} S^+ \quad (\text{S40})$$

where $r = Z_0/z_0 \sim O(1)$, and the rotating-wave approximation enabled by the weak-coupling assumption is employed in the derivation.

Finally, we study the effect of a small driving on the dynamics of the LC resonators for two relevant cases. We start by considering a LC resonator with time-dependent capacitance $C(t) = C[1 + \delta(t)]$ with $\delta(t + 2\pi/\Omega) = \delta(t)$. Under the weak and slow driving assumptions such that $\delta(t) \rightarrow 0$ and $\Omega/\omega_0 \rightarrow 0$, we can rewrite the circuit equation $v/L + \frac{d}{dt}[C(t)v] = 0$ using the complex mode amplitude $\psi(t)$ as

$$\frac{d\psi}{dt} \approx \left[j \left(1 - \frac{1}{2}\delta\right) \omega_0 - \dot{\delta} \right] \psi. \quad (\text{S41})$$

Therefore, the driving could introduce effective gain/loss to the system in addition to modifying the resonant frequency.

Next, we consider the case of two identical LC resonators coupled through a time-modulated capacitance $C_k(t) = C[h_0 + h_1(t)]$, with $h_1(t + 2\pi/\Omega) = h_1(t)$. Like in the previous case, we resort to the approximations $h_1(t) \rightarrow 0$ and $\Omega/\omega_0 \rightarrow 0$, and weak coupling limit $h_0 \rightarrow 0$, which allow us to write the Kirchoff equations as described by Eqs. (S31) and (S32) but replacing $\kappa \rightarrow h(t) = h_0 + h_1(t)$. Introducing the complex mode amplitudes ψ_1 and ψ_2 ,

$$\frac{d\psi_1}{dt} \approx j\omega_0 \left(1 - \tilde{h}(t)\right) \psi_1 + j\omega_0 \tilde{h}(t) \psi_2, \quad (\text{S42})$$

$$\frac{d\psi_2}{dt} \approx j\omega_0 \tilde{h}(t) \psi_1 + j\omega_0 \left(1 - \tilde{h}(t)\right) \psi_2, \quad (\text{S43})$$

where $\tilde{h}(t) = \frac{h(t)}{2} - j\frac{\dot{h}(t)}{\omega_0}$. Like in the previous case of the driven LC resonator, the driving of the capacitance introduces effective gain/loss due to the non-zero imaginary part of $\tilde{h}(t)$. But in contrast, the driving of the coupling capacitance not only modulates the coupling but also the resonant frequencies of the resonators.

In the weak coupling limit, above mechanisms can be superimposed on top of each other independently ignoring higher-order effects. For example, using this rule we can write down directly the CME for the circuits as shown in Fig. 1(c,d), where we set $C_n(t) = C[1 + \delta_n(t)]$, $n = 2, 3$, and $C_k(t) = C h(t) = C[h_0 + h_1(t)]$. For simplicity, we consider $h_0 = \kappa$. Explicitly, using the complex mode amplitudes of each resonator $\langle n | \psi \rangle = \psi_n$ and the input/output wave amplitudes $\langle n | S^\pm \rangle = S_n^\pm$, we have

$$\frac{d}{dt} |\psi\rangle = [jH_0(t) - \Gamma] |\psi\rangle + jD^T |S^+\rangle \quad (\text{S44})$$

$$|S^-\rangle = |S^+\rangle + jD |\psi\rangle \quad (\text{S45})$$

where

$$H_0(t) = \omega_0 \begin{bmatrix} w_1 & \frac{\kappa}{2} & \frac{\kappa}{2} \\ \frac{\kappa}{2} & w_1 - \frac{\delta_2 + h_1}{2} & \frac{\kappa}{2} + \frac{h_1}{2} \\ \frac{\kappa}{2} & \frac{\kappa}{2} + \frac{h_1}{2} & w_1 - \frac{\delta_3 + h_1}{2} \end{bmatrix}, \quad \Gamma = \frac{1}{2} D^\dagger D + \begin{bmatrix} 0 & 0 & 0 \\ 0 & \dot{\delta}_2 + \dot{h}_1 & -\dot{h}_1 \\ 0 & -\dot{h}_1 & \dot{\delta}_3 + \dot{h}_1 \end{bmatrix}, \quad \text{and } D = \begin{bmatrix} \sqrt{\omega_0 r} \epsilon & 0 & 0 \\ 0 & \sqrt{\omega_0 r} \epsilon & 0 \\ 0 & 0 & \sqrt{\omega_0 r} \epsilon \end{bmatrix}, \quad (\text{S46})$$

with $w_1 = 1 - \kappa - \frac{1}{2}\epsilon$. Note that the precise form of the CMT used in the main text can be obtained by simply letting $|S^\pm\rangle \rightarrow \mp j |S^\pm\rangle$, i.e., a proper redefinition of phase factors.

CALCULATION OF RECTIFICATION USING TIME-MODULATED WHISPERING GALLERY MODE RESONATORS.

Setup.- The photonic circuit considered in our analysis is shown in Fig. S1(a). It consists of three whispering gallery mode resonators (large rings) tuned to resonant wavelength $\lambda_0 \approx 6 \mu\text{m}$ ($f_0 \approx 50 \text{ THz}$) and coupled in a circular-chain manner via smaller racetrack resonators. At the same time, two of the large ring resonators are coupled to straight fiber wave-guides. The core of the ring resonators and fibers has a refractive index $n_{\text{core}}=3$, while the cladding has a refractive index $n_{\text{cladd}}=1.25$. The width of the core is $1.4 \mu\text{m}$, while the width of the cladding is $5.6 \mu\text{m}$. The diameter of the large ring resonators is $31.8 \mu\text{m}$. At the same time, the circular sections of the racetrack resonators have a radius of curvature $3.3 \mu\text{m}$, while the straight sections of the racetrack resonators have a length $8 \mu\text{m}$. The optical length of the racetrack coupling resonators is more than two times smaller than the optical length of the large ring resonators. This configuration allows tuning the system in a way that the resonant modes of the racetrack resonators do not overlap with the resonant mode of the large rings. We chose a wavelength range where the racetrack resonators can be considered as couplers between the large ring resonators.

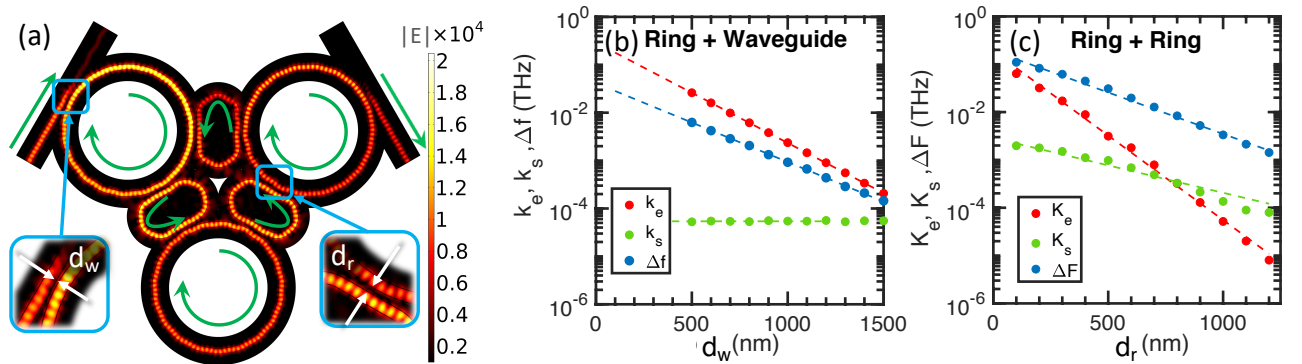


FIG. S1: **Photonic setup.** (a) Colors indicate the electric field intensity inside the three-chain photonic structure. The green arrows indicate the light propagation direction when it travels from the left to the right ports. (b) The coupling parameter k_e (red dots), scattering losses k_s (blue dots), and frequency shift Δf (green dots) of the ring coupled to a straight fiber wave-guide as a function of distance between them, d_w . (c) The coupling parameter K_e (red dots), scattering losses K_s (blue dots), and frequency shift ΔF (green dots) of the ring coupled to another ring via a racetrack coupler separated a distance d_r from the resonators. In (b),(c), dashed lines are the exponential fit (see parameters in the main text).

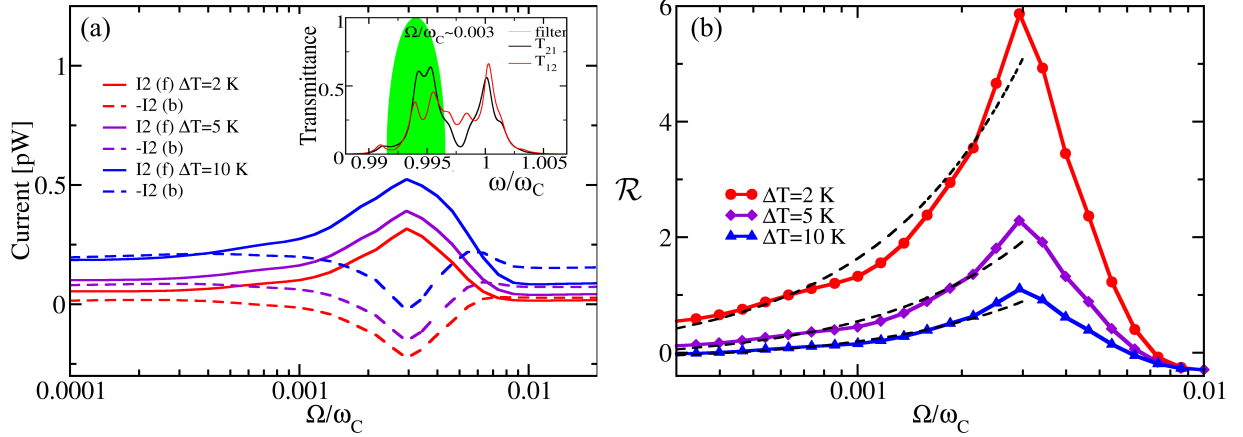


FIG. S2: (a) Currents measured at the right waveguide for the forward, $I_2^{(f)}$ (solid line), and backward, $I_2^{(b)}$ (dashed line), configurations as a function of the modulation frequency Ω for temperature gradients $\Delta T = 2$ K (red), $\Delta T = 5$ K (violet), and $\Delta T = 10$ K (blue), after subtracting a trivial baseline current due to the losses when the rectifier is in the *off-mode*, i.e. $T_C = T_H = 300$ K and absence of modulations, $\delta_0 = 0$. Inset: nonreciprocal transmittances for $\Omega/\omega_C \approx 0.003$, $\delta_0/\omega_C = 0.005$ and the engineered emission filter, Eq. (10), with parameters $\omega^*/\omega_0 = 0.9925$ and $b = 0.0025$. (b) The corresponding rectification parameter for the three temperature gradients (solid lines with symbols). The dashed lines are functions of the form $R = \alpha \times (\Omega/\Delta T) + R_0$ with $\alpha = 3450$ the best fit parameter. Parameters: $d_r = 100$ nm, $d_w = 400$ nm, $\omega_C/(2\pi f_0) = 0.998$

In order to extract the coupling coefficients for the CMT analysis, we run two separate FEM simulations using COMSOL multiphysics software: one for the large ring, coupled to a straight waveguide. The other simulation involves a ring resonator coupled to another large ring via the racetrack resonator. In the simulations, we assumed scattering boundary conditions at the boundaries of the fiber cladding.

The transmission through the fiber with a coupled ring, according to the CMT, is given by [S9]:

$$T(f) = \left| 1 - \frac{\kappa_e}{k_e/2 + (\kappa_s + \kappa_i)/2 + i(f - f_0)} \right|^2, \quad (\text{S47})$$

where κ_e denotes the extrinsic coupling coefficient (determining the light transfer between the ring and another ring/fiber), κ_s denotes the scattering losses due to evanescent coupling and intrinsic losses from the coupler. Finally, κ_i denotes the intrinsic losses of the large ring resonator due to the leakage of the light. The resonant frequency of the large ring is indicated as f_0 .

The best fitting of the transmittance curve achieved from FEM simulations, with Eq. (S47), allows us to extract all the coupling parameters of our setup. To further optimize the setup, we run FEM simulations of the single ring coupled to a straight waveguide for a wide range of coupling distances d_w (see the left inset on Fig. S1(a) between the fiber and the ring). In Fig. S1(b), we report the extracted coupling strength $k_e = \kappa_e$ (red dots), combined losses $k_s = \kappa_s + \kappa_i$ (green dots), and frequency shift $\Delta f = f_0(d_w) - f_0$ (blue dots) of the ring coupled to a straight waveguide. The achieved coupling parameters and frequency detuning were then fitted with exponential functions of the form $a \cdot e^{(-b \cdot d_w)}$ (see dashed lines on Fig. S1(b)). We found that $k_e = 0.29 \cdot e^{-(0.048 \cdot d_w [\text{nm}])}$ THz, $k_s = 5.4 \cdot 10^{-5}$ THz and is almost constant, while $\Delta f = 0.041 \cdot e^{-(0.038 \cdot d_w [\text{nm}])}$ THz and $f_0 = 49.75$ THz.

Similarly, the transmittance for the large ring coupled to another large ring via a racetrack coupler was simulated for various distances d_r between the large ring and a racetrack resonator (see the right inset on Fig. S1(a)). It was then fitted with the Eq. (S47), which allowed us to extract the intra-ring coupling coefficients (see Fig. S1(c): $K_e = \kappa_e$ (red dots), combined losses $K_s = \kappa_s + \kappa_i$ (green dots) and frequency shift $\Delta F = f_0(d_r) - f_0$ (blue dots) as a function of d_r . The coupling parameters were fitted with the exponential function of distance d_r (see dashed lines on Fig. S1(c)) resulting in $K_e = 0.19 \cdot e^{-(0.008 \cdot d_r [\text{nm}])}$ THz, $K_s = 0.003 \cdot e^{-(0.0026 \cdot d_r [\text{nm}])}$ THz, and $\Delta F = 0.19 \cdot e^{-(0.004 \cdot d_r [\text{nm}])}$ THz, with $f_0 = 49.75$ THz.

Currents and rectification.- Based on the parameters extracted above, we build the associated Temporal Coupled Mode Theory (CMT), Eqs. (1) and (9) of the main text, to describe the time-dependence of the modal amplitudes of the three large resonators, while the small racetrack resonators act only as couplers. The coupling between

each pair of resonators is represented by the coupling strength K_e . The decay rates of the resonators are $\gamma_{1(2)} = (1/2)[k_e + k_s + 2(K_s - \kappa_i)]$, and $\gamma_3 = (1/2)[\kappa_i + 2(K_s - \kappa_i)]$, which are associated to the proximity of the waveguide and/or the couplers and to the intrinsic loss rate k_i . Only the rate $k_e/2$ is associated to radiation from the waveguides and satisfies the fluctuation-dissipation relation resulting in $D_{n,\beta} = \sqrt{k_e}\delta_{n,\beta}$ [see Eq. (1) of the main text], where $\beta = 1, 2$ is the index of reservoir. We verified that all the decay rates or the coupling K_e do not change significantly when changing the frequency of the resonators.

For this setup, we only consider modulation of the large resonators as opposed to the driving protocol of the main text where we have modulated also the coupling. Specifically, the resonant frequencies, which are shifted by the proximity of the waveguide and/or the two couplers, are $\omega_{1(2)}/(2\pi) = f_0 + \Delta f + 2\Delta F + \delta_0/(2\pi)\cos(\Omega t + \phi_{1(2)})$, $\omega_3/(2\pi) = f_0 + 2\Delta F + \delta_0/(2\pi)\cos(\Omega t + \phi_3)$ where Ω and δ_0 are the modulation frequency and amplitude, and the phases $\phi_n = (2/3)\pi(n-1)$. Such a driving scheme is inspired from Ref. [S10], where the time-modulation induces angular momentum biasing. We have confirmed that this modulation produces nonreciprocal transmittances $\mathcal{T}_{1,2}^F(\omega) \neq \mathcal{T}_{2,1}^F(\omega)$, as reported in the inset of Fig. S2(a).

We consider thermal reservoirs emitting thermal radiation that enters the structure via the waveguides. In Fig. S2(a), we report the currents at the right waveguide for the forward, $\bar{I}_2^{(f)}$, and backward, $\bar{I}_2^{(b)}$, configurations, after subtracting a trivial baseline current due to the losses when the rectifier is in the *off-mode*, i.e. $T_C = T_H = 300$ K and in the absence of modulations, $\delta_0 = 0$. The filtering function Eq. (10), is now centered at $\omega^*/\omega_0 = 0.9925$ with $b = 0.0025$. We observe that, as Ω increases, the radiated current becomes non-reciprocal.

In Fig. S2(b), we report the associated rectification parameter \mathcal{R} as a function of Ω for three temperature gradients. We have found that the rectification increases linearly with $(\Omega/\Delta T)$, following the predictions of Eq. (8) of the main text, i.e. $\mathcal{R} \sim \alpha(\Omega/\Delta T)$ where $\alpha \approx 3450$ is a best fitting parameter (see black dashed lines). For larger driving frequencies, the linear response theory prediction of Eq. (8) is not applicable. Instead, we find that the rectification factor \mathcal{R} reaches a maximum value when the modulation frequency Ω favors transitions between the (quasi) reciprocal channel, ω_C , and the (mean) frequency of the counter-rotating super-modes, $\omega_{L(R)}$, i.e. $\Omega \approx \omega_C - \omega_{L(R)} = 3\kappa \approx 0.005\omega_C$. In fact, as discussed in the main text, for such frequency driving, the system demonstrates refrigeration indicated by the fact that $|\mathcal{R}| > 1$.

FDTD SIMULATION OF A TIME-MODULATED SILICON WHISPERING GALLERY MODE RESONATOR.

To demonstrate the feasibility of the proposed approach, we also performed finite-difference time-domain (FDTD) simulations of a simpler, but yet realistic, photonic setup shown in Fig. S3(a). It consists of a silicon whispering gallery mode (WGM) resonator, which has three sections (labeled with 1, 2, 3 in Fig. S3(a), where the dielectric permittivity of each section is periodically modulated such that $\varepsilon_i(t) = \varepsilon_{Si} + \Delta\varepsilon_i(t)$, where $\Delta\varepsilon_i(t) = \Delta\varepsilon_m \cdot \cos(\Omega t + \frac{2\pi}{3}(i-2))$ and $\varepsilon_{Si} = 12$ is the dielectric permittivity of Silicon. Here the $\varepsilon_m = 5 \cdot 10^{-3} \cdot \varepsilon_{Si}$ and Ω is the modulation frequency.

The WGM ring resonator is evanescently coupled to a pair of waveguides such that the structure has four ports, as indicated in Fig. S3(a). We assume that thermal baths are connected to ports 1 and 2, while excitations escaping the structure through ports 3 and 4 are considered as losses. Here $\omega_c = 2\pi\frac{C}{\lambda_c}$, where C is the speed of light and $\lambda_c = 1550$ nm is a reference wavelength.

We show that the time dependent modulation produces extreme non-reciprocity in transport. This can be observed from Figs. S3(b) and (c). In Fig. S3(b), one can see the $|E|^2$ field profile at frequency $\omega = 0.70718\omega_c$, for the case of port 1 and port 2 connected to the hot ($T_H > 0$ K) and cold ($T_C = 0$ K) reservoirs, respectively. From Fig. S3(b), we observe that the WGM resonator with periodically modulated permittivity does not transmit radiation from the port 1 to the port 2. In Fig. S3(c), port 2 is connected to the hot bath while port 1 is connected to the cold bath. In contrast with the previous case shown in Fig. S3(b), here we observe that the same permittivity modulation results in almost perfect propagation of radiation from the port 2 to the port 1.

To further study the rectification of the photonic setup at different modulation parameters, we run FDTD simulations for a broadband frequency range in the vicinity of the frequency $\omega = 0.70718\omega_c$. The transmittance spectrum from the port 1 to the port 2 (\mathcal{T}_{21}) and transmittance spectrum from the port 2 to the port 1 (\mathcal{T}_{12}) are shown on Fig. S4(a)-(c) for different values of modulation frequency Ω , demonstrating highly nonreciprocal transport. The associated thermal currents, $\bar{I}_2^{(f)}$ and $\bar{I}_2^{(b)}$, are reported in Fig. S4(d) for various modulation frequencies Ω . For the calculation of such currents, we used the spectral filtering window indicated with green regions in Figs. S4(a)-(c) and it was assumed that $T_C = 300$ K and $T_H = T_C + \Delta T$ ($\Delta T = 10$ K).

Next, we use the extracted currents, $\bar{I}_2^{(f)}(\Omega)$ and $\bar{I}_2^{(b)}(\Omega)$, to calculate the rectification parameter $\mathcal{R}(\Omega)$ for a range of

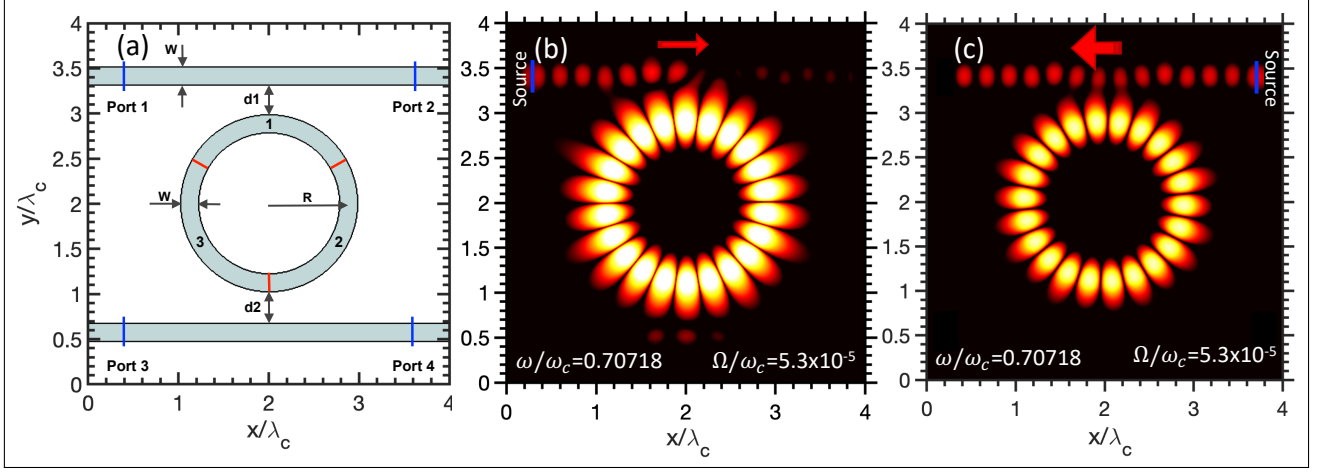


FIG. S3: (a) A schematic of the photonic setup used in the FDTD simulations. It consists of a whispering gallery mode (WGM) resonator having three equal sections (1-3) with modulated permittivity and it is coupled to a pair of wave-guides. The radius of the WGM resonator is $R = 0.88\lambda_c$ and the width of the WGM resonator and wave-guides is $W = 0.2\lambda_c$. The distance to the first wave-guide with port 1 and port 2 is $d_1 = 0.33\lambda_c$, while the distance to the second wave-guide is $d_2 = 0.35\lambda_c$, where $\lambda_c = 1550$ nm is the reference wavelength. (b) and (c) The $|E|^2$ field profile of the modulated photonic setup shown in panel (a) with modulation frequency $\Omega = 5.3 \cdot 10^{-5}\omega_c$ when a source of waves with frequency $\omega = 0.70718\omega_c$ is placed at port 1 (b) or port 2 (c).

modulation frequencies Ω , as show on Fig. S4(e). Here, we find that, for slow modulation frequencies, the rectification parameter $\mathcal{R}(\Omega)$ grows linearly as modulation frequency Ω increases, as indicated by the linear fitting function (dashed blue line) in Fig. S4(e), thus verifying the theoretical prediction of the main text.

-
- [S1] L. J. Fernández-Alcázar, H. Li, M. Nafari, T. Kottos. *To be published*.
[S2] H Li, L. J. Fernández-Alcázar, F. Ellis, B. Shapiro, T. Kottos, *Adiabatic Thermal Radiation Pumps for Thermal Photonics*, Phys. Rev. Lett. **123**, 165901 (2019).
[S3] H. Li, B. Shapiro, T. Kottos, *Floquet scattering theory based on effective Hamiltonians of driven systems*, Phys. Rev. B **98**, 121101(R) (2018).
[S4] H. Li, T. Kottos, *Design Algorithms of Driving-Induced Nonreciprocal Components*, Phys. Rev. Applied **11**, 034017 (2019).
[S5] S. Buddhiraju, W. Li, S. Fan, *Photonic Refrigeration from Time-Modulated Thermal Emission*, Phys. Rev. Lett. **124**, 077402 (2020).
[S6] E. Domany, S. Alexander, D. Bensimon, L.P. Kadanoff, *Solutions to the Schrödinger equation on some fractal lattices*, Phys. Rev. B **28**, 3110 (1983).
[S7] H. M. Pastawski and E. Medina, *Tight Binding methods in quantum transport through molecules and small devices: From the coherent to the decoherent description*, Rev. Mex. Fis. **47S1**, 1 (2001).
[S8] C. J. Cattena, L. J. Fernández-Alcázar, R. A. Bustos-Marín, D. Nozaki, and H. M. Pastawski, *Generalized multi-terminal decoherent transport: recursive algorithms and applications to SASER and giant magnetoresistance*, J. Phys.: Condens. Matter **26**, 345304 (2014).
[S9] Y. L. Li and P. F. Barker, *Characterization and Testing of a Micro-g Whispering Gallery Mode Optomechanical Accelerometer*, Journal of Lightwave Technology **36**, 3919 (2018).
[S10] N. Estep, D. Sounas, J. Soric, A. Alù, *Magnetic-free non-reciprocity and isolation based on parametrically modulated coupled-resonator loops*, Nat. Phys. **10**, 923 (2014).

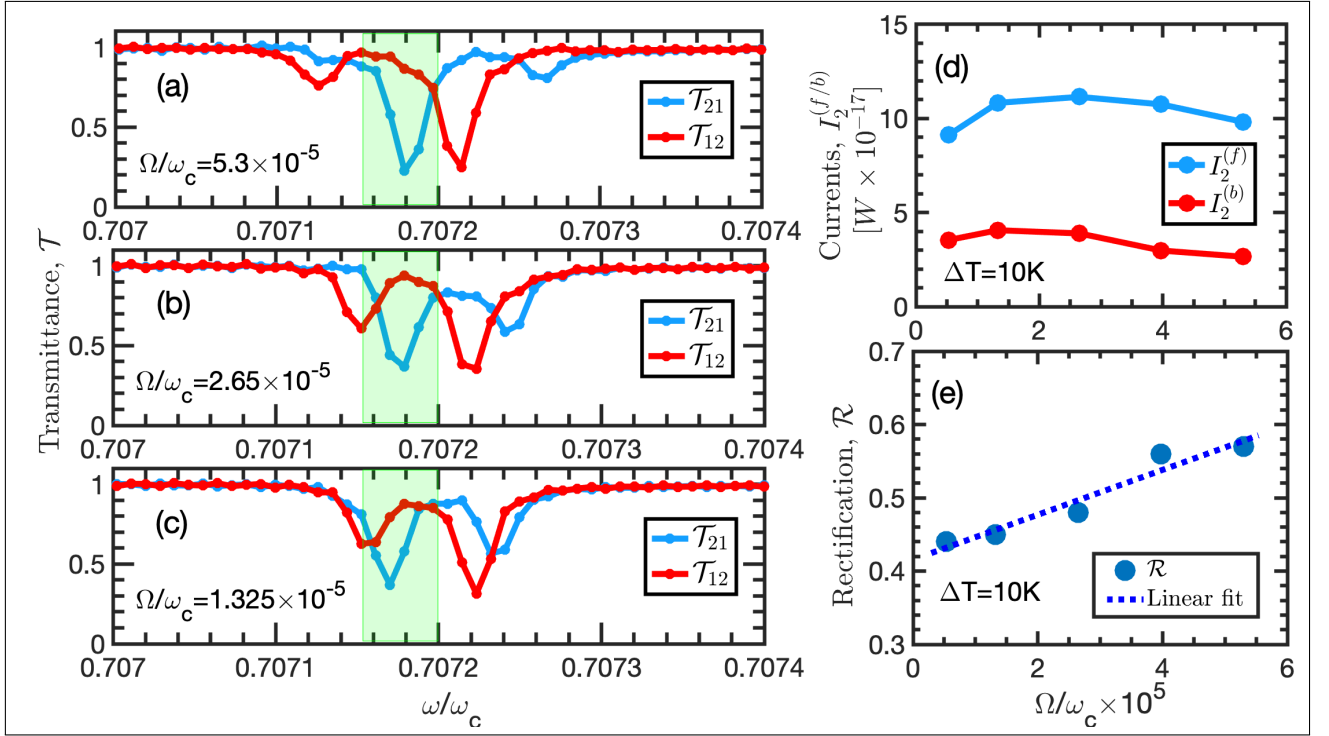


FIG. S4: FDTD simulations. Transmittance spectra \mathcal{T}_{21} from the port 1 to port 2 (blue line) and \mathcal{T}_{12} from the port 2 to port 1 (red line), when the WGM ring permittivity is modulated with frequency $\Omega = 5.3 \cdot 10^{-5} \omega_c$ (a), $\Omega = 2.65 \cdot 10^{-5} \omega_c$ (b), and $\Omega = 1.325 \cdot 10^{-5} \omega_c$ (c). The green domain on panels (a)-(c) indicates the spectral filtering window. (d) Thermal energy currents \bar{I}_2^f (blue line) and \bar{I}_2^b (red line) calculated in the vicinity of the port 2 for various values of the modulation frequency Ω using the spectral filtering window shown on panels (a)-(c). (e) Rectification parameter \mathcal{R} (blue dots) calculated from the currents \bar{I}_2^f and \bar{I}_2^b for various values of the modulation frequency Ω . The blue dashed line indicates the numerical fit with a linear function.